

See discussions, stats, and author profiles for this publication at: <https://www.researchgate.net/publication/235751324>

Structural and Conducting Features of Niobium-Doped Lanthanum Tungstate, La₂₇(W_{1-x}Nb_x)₅O_{55.55-δ}

ARTICLE in CHEMISTRY OF MATERIALS · FEBRUARY 2013

Impact Factor: 8.35 · DOI: 10.1021/cm304067d

CITATIONS

13

READS

28

7 AUTHORS, INCLUDING:



D. Marrero-López

University of Malaga

132 PUBLICATIONS 2,363 CITATIONS

[SEE PROFILE](#)



Laura Leon-Reina

University of Malaga

48 PUBLICATIONS 940 CITATIONS

[SEE PROFILE](#)



Jesús Canales-Vázquez

University of Castilla-La Mancha

108 PUBLICATIONS 3,094 CITATIONS

[SEE PROFILE](#)



Miguel A. G. Aranda

ALBA synchrotron Light Source - Barcelona, S...

257 PUBLICATIONS 5,503 CITATIONS

[SEE PROFILE](#)

Structural and Conducting Features of Niobium-Doped Lanthanum Tungstate, $\text{La}_{27}(\text{W}_{1-x}\text{Nb}_x)_5\text{O}_{55.55-\delta}$

M. J. Zayas-Rey,[†] L. dos Santos-Gómez,[†] D. Marrero-López,[‡] L. León-Reina,[§] J. Canales-Vázquez,^{||}
M. A. G. Aranda,^{†,⊥} and E. R. Losilla*,[†]

[†]Department of Inorganic Chemistry, [‡]Department of Applied Physics I, Laboratory of Materials and Surfaces, and [§]Servicios Centrales de Apoyo a la Investigación, University of Málaga, 29071 Málaga, Spain

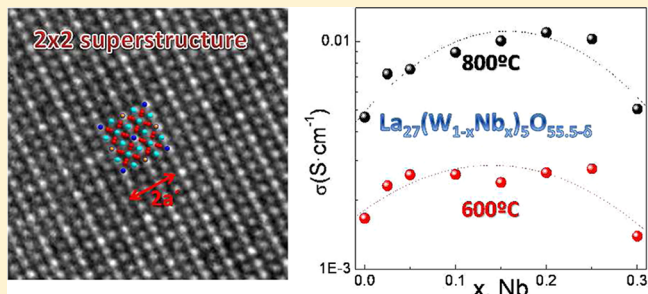
^{||}Renewable Energy Research Institute, University of Castilla-La Mancha, 02071 Albacete, Spain

[⊥]CELLS-ALBA Synchrotron, Carretera BP 1413, Km. 3.3, E-08290 Cerdanyola, Barcelona, Spain

Supporting Information

ABSTRACT: The most studied ceramic proton conductors are those based on the perovskite structure. However, these materials have some practical drawbacks including their poor tolerance to carbonation. Hence, proton-conducting ceramic materials with fluorite structure are currently under investigation. One of the most studied materials is the lanthanum tungstate, “ $\text{Ln}_6\text{WO}_{12}$ ”. Here, we report a new series of compounds $\text{La}_{27}\text{W}_{5-5x}\text{Nb}_{5x}\text{O}_{55.5-5x/2}\square_{8.5+5x/2}$ obtained by niobium doping to optimize/increase the amount of oxygen vacancies. The limiting composition has been established as $\text{La}_{27}\text{NbW}_4\text{O}_{55.0}\square_{9.0}$ with an astonishing 14% of oxygen vacancies. The materials have been studied by Rietveld analysis of high-resolution laboratory X-ray powder diffraction data and electron microscopy. Thermal analysis measurements in a wet atmosphere indirectly confirm the increase of oxygen vacancies as the amount of incorporated protons increases with the niobium content. A thorough electrical characterization has been carried out including overall conductivity measurements in wet and dried atmospheres, conductivity as a function of the oxygen partial pressure, and electronic contribution by the Hebb–Wagner polarization method. The data collected suggest that the proton conductivity is dominant below 600 °C. However, above 800 °C the conductivity values are almost independent of the water partial pressure which indicates that the oxide ion is the main charge carrier. The highest conductivity value was measured for $\text{La}_{27}\text{NbW}_4\text{O}_{55}$, i.e., 0.01 S·cm⁻¹ at 800 °C compared to 0.004 S·cm⁻¹ for the nonsubstituted material $\text{La}_{27}\text{W}_5\text{O}_{55.5}$. At temperatures below 800 °C, these materials are nearly pure ionic conductors with transport numbers higher than 0.98, while at higher temperatures these compounds are mixed ionic–electronic conductors displaying both n- and p-type electronic contributions.

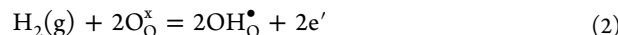
KEYWORDS: $\text{La}_6\text{WO}_{12}$, $\text{La}_{27}(\text{W}_{1-x}\text{Nb}_x)_5\text{O}_{55.5-\delta}$, fluorite structure, PC-SOFC, ionic and electronic conductivity



1. INTRODUCTION

Oxides that exhibit significant proton conductivity at elevated temperatures are candidates for different electrochemical applications, such as hydrogen sensors, membranes for hydrogen production, and proton conducting solid oxide fuel cells (PC-SOFC).^{1–5}

The most studied ceramic proton conductors are those based on cerates BaCeO_3 and zirconates BaZrO_3 with perovskite type structure (ABO_3). Oxygen vacancies are introduced into the perovskite structure by aliovalent doping, that is, partial replacement of cerium or zirconium by Y^{3+} , Yb^{3+} , Gd^{3+} , Nd^{3+} , etc.^{6–12} The proton conduction in these materials occurs either via the hydration of oxygen vacancies after the material is exposed to water-containing atmospheres (eq 1) and/or by reduction of oxide ions in the lattice (eq 2).



However, these materials show several drawbacks for practical applications. For instance, cerates exhibit poor tolerance to carbonation due to the basicity of the alkaline-earth cation. Proton conductors based on BaZrO_3 show better chemical stability against the carbonation, though require very high sintering temperatures (~1700 °C) to obtain dense ceramics. In addition, the high grain boundary resistance of these materials decreases the overall conductivity and hence their performances.

Alternative proton-conducting materials with non perovskite-based structures are being studied to overcome these

Received: November 7, 2012

Revised: January 8, 2013

Published: January 8, 2013

drawbacks. Rare-earth tungstates with general composition “ $\text{Ln}_6\text{WO}_{12}$ ” have attracted attention in the past few years due to their relatively high mixed proton–electron conductivity.^{13–20} The proton conductivity is predominant at temperatures lower than 800 °C with a maximum conductivity value of $\sim 3 \times 10^{-3}$ S/cm at 800 °C for a composition close to $\text{La}_6\text{WO}_{12}$. At high temperatures, these materials are mixed ionic-electronic conductors exhibiting n- and p-type electronic conductivity under reducing and oxidizing atmospheres, respectively. One of the main advantages of these materials is that they present high tolerance toward CO_2 and H_2S environments above 650 °C^{21,22} in contrast to alkaline-earth containing perovskites. Therefore, this material is an appealing candidate²³ for PC-SOFC components.

The series of compounds $\text{La}_{6-y}\text{WO}_{12-\delta}$ $0 \leq y \leq 0.12$ was studied by neutron and synchrotron powder diffraction.^{19,24} They crystallize in a fluorite-related cubic superstructure with $\bar{F}\bar{4}3m$ space group. On the basis of the crystalchemistry study, the composition of the series can be written as $\text{La}_{28-y}\text{W}_{4+y}\text{O}_{54+\delta}\square_{10-\delta}$ (LWO), where tungsten partially occupies the lanthanum sites and the oxygen vacancy concentration ($\square = 10 - \delta$; $\delta = 3y/2$) increases for lower tungsten contents.^{19,20} The solid solution in the $\text{La}_{28-y}\text{W}_{4+y}\text{O}_{54+\delta}\square_{10-\delta}$ series was found for La/W ratio between 5.3 ($y \sim 1.08$) and 5.7 ($y \sim 0.78$), and outside this compositional range, secondary phase segregations were detected. Hence, the lanthanum tungstate with $\text{La}/\text{W} = 6.0$ composition, usually written as “ $\text{La}_6\text{WO}_{12}$ ”, cannot be considered as a single phase material.¹⁹ Furthermore, the highest oxygen vacancy concentration is found for $\text{La}_{27.22}\text{W}_{4.78}\text{O}_{55.17}\square_{8.83}$ ($y \sim 0.78$).

The structure of LWO is shown in Figure 1; the lanthanum ions are coordinated with eight oxygen atoms: the La(4a) forms

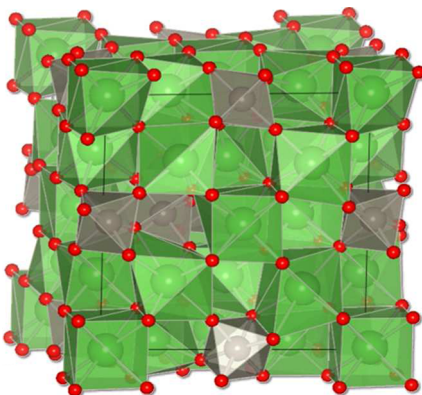


Figure 1. Crystal structure of $\text{La}_{28-y}\text{W}_{4+y}\text{O}_{54+\delta}$ (for $y = 1$) extracted from.²⁴

relatively regular LaO_8 cubes, while La(24g) has a more distorted environment. W(4b) sites are fully occupied in octahedral coordination, and the extra W(24g) are located on the lanthanum sites.

Very recently, molybdenum substituted lanthanum tungstates,²⁵ $\text{La}_{28-y}(\text{W}_{1-x}\text{Mo}_x)_{4+y}\text{O}_{54+\delta}$ ($x = 0-1$, $y = 0.923$) were investigated seeking for an enhancement of the electronic conductivity for its use as a mixed electron–proton conductor in hydrogen gas separation membrane applications. The electronic conductivity was enhanced substantially, without altering significantly the proton conductivity, due to the easier reduction of Mo^{6+} compared to the nonsubstituted material.

Aliovalent doping in $\text{La}_{28-y}\text{W}_{4+y}\text{O}_{54+\delta}\square_{10-\delta}$ might lead to an improvement of the ionic conductivity. In this sense, in this work, a new series of compounds, $\text{La}_{27}\text{W}_{5.5-x}\text{Nb}_{5x}\text{O}_{55.5-5x/2-\delta}$ ($x = 0.0, 0.025, 0.05, 0.10, 0.15, 0.20, 0.25$, and 0.30) was prepared by partial substitution of W^{6+} by Nb^{5+} in order to increase the concentration of oxygen vacancies and to study their effect on the structural and transport properties. To the best of our knowledge, oxygen vacancies by aliovalent doping into LWO framework has not been reported to date. High resolution laboratory X-ray powder diffraction (LXRPD) and transmission electron microscopy (HRTEM) were used to investigate the crystal structure. Electrochemical characterization allowed establishing the nature of the conductivity, highlighting the contributions of the proton and electronic charge carriers.

2. EXPERIMENTAL SECTION

Synthesis of Powders. Materials with composition $\text{La}_{27}(\text{W}_{1-x}\text{Nb}_x)_5\text{O}_{55.5-5x/2}$ ($x = 0.0, 0.025, 0.05, 0.10, 0.15, 0.20, 0.25$, and 0.30) were prepared by a freeze-drying precursor method from an aqueous cation solution with ethylenediaminetetraacetic acid (EDTA) as complexing agent. The $\text{La}_{27}/(\text{W} + \text{Nb})_5$ ratio was fixed to 5.4 to avoid lanthanum oxide segregation based on an earlier report.¹⁹ Starting materials used as reagents were La_2O_3 (99.99%, Aldrich), WO_3 (99.99%, Aldrich), $\text{Nb}(\text{HC}_2\text{O}_4)_5\cdot\text{H}_2\text{C}_2\text{O}_4$ (97%, ABCR), and EDTA (99.5%, Aldrich). Lanthanum oxide was precalcined at 1000 °C for 2 h in order to achieve dehydration and decarbonation. Precursor solutions were prepared separately by dissolving $\text{Nb}(\text{HC}_2\text{O}_4)_5\cdot\text{H}_2\text{C}_2\text{O}_4$ in distilled water, La_2O_3 in hot diluted nitric acid, and WO_3 in diluted ammonia. An EDTA solution was added as complexing agent in a 1:1 ligand/metal molar ratio. The different cation solutions were mixed in stoichiometric relations and stirred for 15 min, and the pH was adjusted to 8–9 by ammonia addition, resulting in a homogeneous and transparent solution. The volume and the cation concentration of the resulting solutions were 100 mL and 0.01 M of La^{3+} , respectively. The solutions were dropped and frozen in liquid nitrogen and then dehydrated by vacuum sublimation in a Telstar Cryodos freeze-dryer for 2 days. The amorphous precursor powders were immediately calcined at 300 °C to prevent rehydration and then fired at 800 °C for 1 h to remove the residual organic species and achieve crystallization. These powders were pressed into pellets and fired between 1400 and 1600 °C for 4 h. After that the pellets were ground and further characterized by different methods. For simplicity, the $\text{La}_{27}(\text{W}_{1-x}\text{Nb}_x)_5\text{O}_{55.5-\delta}$ samples are hereafter labeled as Nb_x , where x is the niobium content.

Characterization of Powders. All compounds were characterized by laboratory X-ray powder diffraction (LXRPD) at room temperature. The powder patterns were collected on a PANalytical X’Pert Pro MPD automated diffractometer (PANalytical) equipped with a Ge(111) primary monochromator and the X’Celerator detector. The overall measurement time was approximately 4 h per pattern to have good statistics over the 10–140° (2θ) angular range, with 0.017° step size. Structural analyses were performed using the GSAS suite of programs.²⁶

Selected area electron diffraction (SAED) and high resolution transmission electron microscopy (HRTEM) imaging were performed on a JEOL JEM 2100 electron microscope equipped with a ($\pm 20^\circ$) double-tilt sample holder, operating at 200 kV. Samples for TEM observation were prepared by dispersion of a very fine ground powder specimen onto a perforated carbon film supported on a Cu grid. HRTEM images were recorded using an Orius Gatan CCD camera (2 × 2 MPi).

Thermogravimetric analysis (TGA) data were recorded on a SDT-Q600 analyzer (TA Instruments) at a heating/cooling rate of 10 °C·min⁻¹ under wet (~3% H_2O) nitrogen.

Sintering Conditions, Microstructural Characterization, and Electrical Measurements. Dense ceramic pellets (~98% of relative density) were obtained by uniaxial pressure of powders in a disk of 10 mm diameter and ~1 mm thickness at 100 MPa. The pellets were

sintered at 1500 °C for $x \leq 0.15$ and 1600 °C for $x \geq 0.20$ for 4 h using heating rates of 5 °C·min⁻¹. The microstructure of the ceramics was observed by scanning electron microscope (SEM) (Jeol JSM-6490LV) combined with energy dispersive spectroscopy (EDS). Platinum electrodes were made by coating pellet faces with METALOR 6082 platinum ink and gradually heating to 800 °C for 15 min at a rate of 10 °C·min⁻¹ in air to decompose the paste and harden the Pt residue. Consecutive treatments were made to achieve an electrical resistance on both pellet faces lower than 1 Ω. Impedance spectra were obtained using a frequency response analyzer (Solartron 1260) in different dry and wet gases (N₂, O₂, and 5% H₂-Ar) in the 0.1 Hz to 1 MHz frequency range with an ac perturbation of 100 mV. The spectra were recorded upon cooling from 900 to 150 °C with a stabilization time of 10 min between consecutive measurements. Impedance spectra were analyzed with the ZView program.²⁷ The resistance and capacitance values of the different contributions were obtained by fitting the impedance spectra data with equivalent circuits. The equivalent circuit consisted of (RQ) elements in series, where R is a resistance and Q is a pseudocapacitance in parallel.

The overall conductivity as a function of oxygen partial pressure [p(O₂) from air to $\sim 10^{-20}$ atm] experiments were performed in a closed tube furnace cell. The p(O₂) values were monitored by using a YSZ oxygen sensor, placed next to the pellet in the cell. The conductivity was continuously recorded as a function of p(O₂). The process consisted of flushing the system with dry 5%H₂-Ar gas mixture at 800, 900, and 1000 °C to reach a minimum in oxygen activity inside the furnace and to ensure that the sample was close to the equilibrium. Then, the gas flow was switched off and the oxygen partial pressure slowly recovers to atmospheric pressure by free diffusion, since the system is not fully airtight. Each isothermal cycle took over 36 h to complete.

The partial electronic contribution to the overall conductivity was determined by the Hebb-Wagner polarization method. A detailed description of this technique can be found elsewhere.^{28,29}

3. RESULTS AND DISCUSSION

Synthesis and Phase Existence. Selected LXRPD patterns of the La₂₇(W_{1-x}Nb_x)₅O_{55.5-5x/2} (0 ≤ x ≤ 0.3) series at different temperatures are shown in Figure 2.

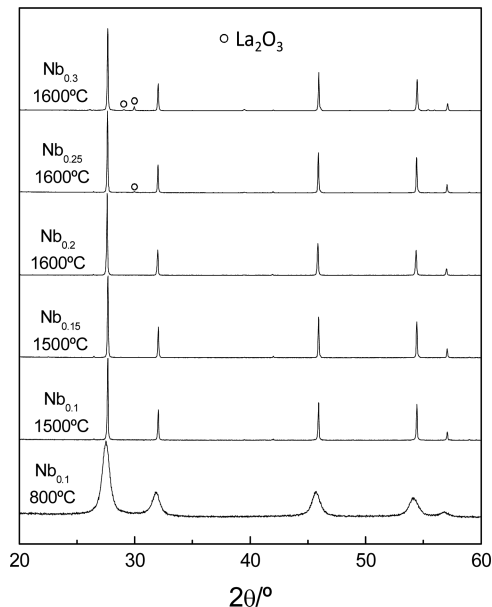


Figure 2. Selected LXRPD patterns for the series La₂₇(W_{1-x}Nb_x)₅O_{55.5-5x/2} (0.0 ≤ x ≤ 0.30) sintered in a range of temperatures.

The compounds are crystalline after sintering at 800 °C, although the LXRPD patterns show considerable peak broadening due to the nanometric nature of the powders with an average crystallite size close to 5 nm. In order to improve the crystallinity and facilitate the structural characterization, the materials were sintered at higher temperatures between 1400 and 1600 °C for 4 h. It should be noted that the sintering temperature necessary to obtain a single phase increases with increasing the Nb content, that is, 1500 °C for $x \leq 0.15$ and 1600 °C for $x \geq 0.2$. This trend is similar to that reported previously for the La_{28-y}W_{4+y}O_{54+y} series, where samples with higher lanthanum content and oxygen vacancy concentration required a higher sintering temperature to produce a single phase.¹⁹ Atomistic simulations also suggested that the structure is more stable with lower concentration of oxygen vacancies; hence, the single phase material can be produced at lower sintering temperatures.²⁴

The analysis of LXRPD data by the Rietveld method shows that materials with Nb content ($x \leq 0.2$) were simple cubic phases. Above that Nb concentration, minor phase segregations corresponding to 2.4(1) and 6.0(1) wt % La₂O₃ appear for Nb_{0.25} and Nb_{0.30} samples, respectively. Hence, the solubility limit of Nb in the La₂₇(W_{1-x}Nb_x)₅O_{55.5-δ} structure is approximately $x = 0.2$.

Structural Analysis. All LXRPD patterns were analyzed by the Rietveld method in the cubic F43m space group using as starting model the structure reported by Magrasó et al. for LWO by neutron powder diffraction.^{19,24} It should be mentioned that a slight distortion from the cubic symmetry was visible for some compositions when using high resolution X-ray synchrotron diffraction,²⁴ and such small distortions are not detected in the present work using LXRPD data.

As a result of the presence of heavy cations with larger scattering factors compared to oxygen, the refinement of the occupation factors cannot be carried out without strong correlations. Therefore, the cation and oxygen contents were fixed to the nominal stoichiometry and distributed as described just below.

For nonsubstituted Nb_{0.0} material, the structural formula, derived from the fluorite-related structure, can be rewritten as La_{1.4}(La_{2.3}W_{2.1})W_{1.4}O_{55.5}□_{8.5}.^{19,24} It is worth highlighting that, in addition to W1, which has an octahedral environment of oxygens due to the vacancies at the O2a and O2b positions, there is also W2 at the La2 position which justifies the overall La/W ratio 5.4 instead of the expected 7.0, which would arise from the nominal stoichiometry "La₂₈W₄O₅₄□₁₀". Our refinement is fully consistent with the previously reported structure;¹⁹ see the first column of Table 1.

In addition, the W/Nb substitution can take place at the W1 or W2 sites; see Table 1. Our refinements are again consistent with Nb⁵⁺ replacing W⁶⁺ at the La2/W2 site. An indirect proof that the Nb/W substitution is mainly occurring at the W2(La2) site rather than at the W1 site is that the series limit is $x = 0.2$, which is the expected for just 1 mol of Nb per 4 mol of W. Higher substitution ratios should be compulsory to the W1 site, but instead, La₂O₃ segregation is observed.

Therefore, the following crystallochemical stoichiometry for the prepared series is proposed: La_{1.4}(La_{2.3}W_{2.1-x}Nb_x)-W_{1.4}O_{55.5-5x/2}□_{8.5+5x/2} with 0.0 ≤ x ≤ 0.20. Final results of the Rietveld refinement are shown in Table 1, and Figure 3 shows an example of the fitting for Nb_{0.10}. The limiting stoichiometry, before phase segregation, is La₂₇NbW₄O_{55.0}□_{9.0}.

Table 1. Unit Cell and Selected Structural Data for $\text{La1}_4(\text{La}_{23}\text{W}_{21-5x}\text{Nb}_{5x})\text{W1}_4\text{O}_{55.5-5x/2}\square_{8.5+5x/2}$ Series from Rietveld Refinement in Space Group $F\bar{4}3m^a$

	Nb _{0.00}	Nb _{0.025}	Nb _{0.05}	Nb _{0.10}	Nb _{0.15}	Nb _{0.20}
<i>a</i> (Å)	11.1812(2)	11.1790(3)	11.1835(2)	11.1819(2)	11.1811(3)	11.1843(3)
<i>V</i> (Å ³)	1397.89(9)	1397.05(1)	1398.73(1)	1398.16(1)	1397.82(1)	1399.02(9)
La1 (4a) @ 000						
Occ. factor	1.0	1.0	1.0	1.0	1.0	1.0
W1 (4d) @ 1/2 1/2 1/2						
Occ. factor	1.0	1.0	1.0	1.0	1.0	1.0
M2 (24g) @ x 1/4 1/4						
La2/W2/Nb, <i>x</i> ~ -0.008						
Occ. factor	0.96/0.04/0.00	0.960/0.035/0.005	0.96/0.03/0.01	0.96/0.02/0.02	0.96/0.01/0.03	0.96/0.00/0.04
O1a (16e) @ xxx, x ~ 0.14						
Occ. factor	1.0	1.0	1.0	1.0	1.0	1.0
O1b (16e) @ xxx, x ~ 0.88						
Occ. factor	1.0	1.0	1.0	1.0	1.0	1.0
O2a (16e) @ xxx, x ~ 0.39						
Occ. factor	0.732	0.731	0.729	0.725	0.721	0.717
O2b (16e) @ xxx, x ~ 0.61						
Occ. factor	0.732	0.731	0.729	0.725	0.721	0.717
<i>R</i> _{wp} (%)	6.34	6.49	6.38	5.98	6.40	6.35
<i>R</i> _F (%)	7.51	7.80	8.48	6.72	7.84	5.95

^aNb_{0.25} and Nb_{0.30} samples are not included as they were not single phase, see text. The reported occupation factors are derived from the nominal compositions and not refined.

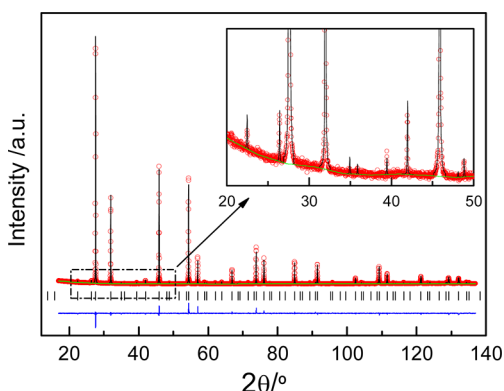


Figure 3. Observed (circles), calculated (solid line), and difference (bottom) LXRDP patterns for the Nb_{0.10} sample, $\text{La1}_4(\text{La}_{23}\text{W}_{20.5}\text{Nb}_{0.5})\text{W1}_4\text{O}_{55.25}\square_{8.75}$.

incorporating slightly higher oxygen vacancy content than $\text{La}_{27.22}\text{W}_{4.78}\text{O}_{55.17}\square_{8.83}$.

The agreement factors reported in Table 1 are acceptable taking into account the degree of atomic disorder in this series.

Neutron diffraction data is required for an accurate determination of the oxygen parameters. Finally, it is worth noting that the cell volume almost does not change with increasing the Nb content. This may be counterintuitive as the ionic radius of niobium, 0.64 Å, is slightly larger than that of tungsten, 0.60 Å (sixfold coordination). However, there is also a change in the oxygen content, Table 1, as the amount of vacancies slightly increases along the series which counterbalances the volume changes and also has important consequences in the thermogravimetric analysis and electrical properties as discussed below. Moreover, although there is not a clear trend in the lattice parameters on increasing Nb content, the crystallographic densities are very similar, ~1%, compared with those measured experimentally for dense ceramic pellets. These densities are plotted in Figure S-1, Supporting Information. This is additional evidence of the Nb incorporation within the frameworks.

Structural Analysis by Electron Diffraction. Selected area electron diffraction (SAED) patterns corresponding to the Nb_{0.15} sample viewed down different zone axes are shown in Figure 4.

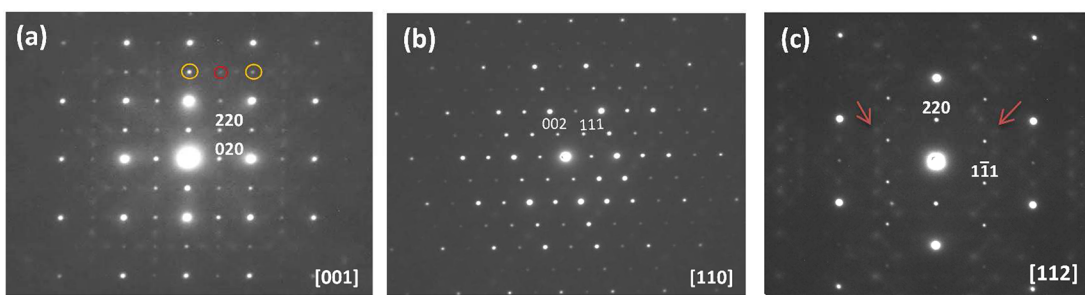


Figure 4. SAED patterns corresponding to the (a) [001], (b) [111], and (c) [112] zone axes, respectively. The patterns could be indexed considering a $2 \times 2 \times 2$ cubic superstructure. The diffraction spots are highlighted with large white dots from the fluorite basic unit cell and small ones from the supercell.

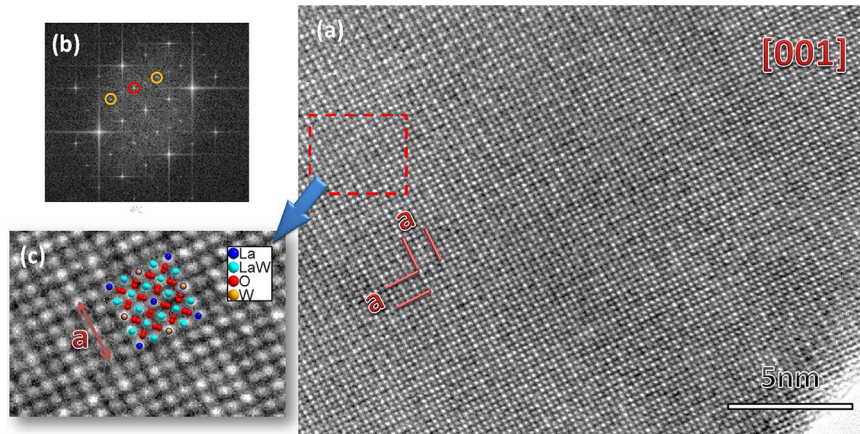


Figure 5. (a) HRTEM images in the [001] zone axes for $\text{Nb}_{0.15}$ showing a 2×2 superstructure, (b) FFT calculated pattern, and (c) a magnification of (a) showing the unit cell atoms.

The SAED pattern recorded down the [001] direction reveals that this material is a cubic $2a' \times 2a' \times 2a'$ superstructure. The main reflections can be indexed according to the cubic unit cell with $a = 2a' = 11.2 \text{ \AA}$ (space group $F\bar{4}3m$) described above. However, extra weak reflections and diffuse scattering are visible along several directions, particularly around the {111} reflections (Figure 4c), which may be ascribed to ordering of oxygen vacancies as usually reported in fluorite-based systems. The HRTEM images show the evidence of a 2×2 superstructure (Figure 5a) which is further confirmed by the FFT calculated pattern and the corresponding IFFT image (Figure 5b,c). In addition the structural data obtained by LXRPD fitted reasonably well to the experimental image, which indicates that the structural model proposed is fairly correct. No significant microstructural changes were found between the samples. Thus the creation of oxygen vacancies after the incorporation of Nb^{5+} in the LWO structure do not affect considerably the microstructure of these materials.

Thermogravimetric Analysis. All samples were studied by thermogravimetric analysis to evaluate the influence of Nb substitution and the consequent increase of vacancy concentration on the incorporation of water in the structure. Water uptake depends on the available oxygen vacancies in the structure and therefore differences are expected depending on the Nb content. The thermogravimetric measurements collected under humidified air showed reproducible curves on both cooling and heating cycles (not shown). Only the curves taken on the cooling processes are compared for the different compositions in Figure 6.

The curves show the typical behavior of a proton conducting material with weight increase upon cooling due to water uptake and the formation of protonic defects, according to the hydration of oxygen vacancies (eq 1).

For these samples the water uptake increases with the Nb content from 0.24 wt % for $\text{Nb}_{0.0}$ to 0.40 wt % for $\text{Nb}_{0.20}$ due to the larger concentration of oxygen vacancies on the oxygen sublattice. A close to linear relationship between the water uptake and the Nb content is shown in the inset of Figure 6. These results further confirm that Nb is incorporated in the lanthanum tungstate structure with the concomitant oxygen vacancy increase.

Electrical Characterization. Sintering and Microstructure. The sintering conditions used to prepare the ceramic pellets led to very dense specimens with relative densities

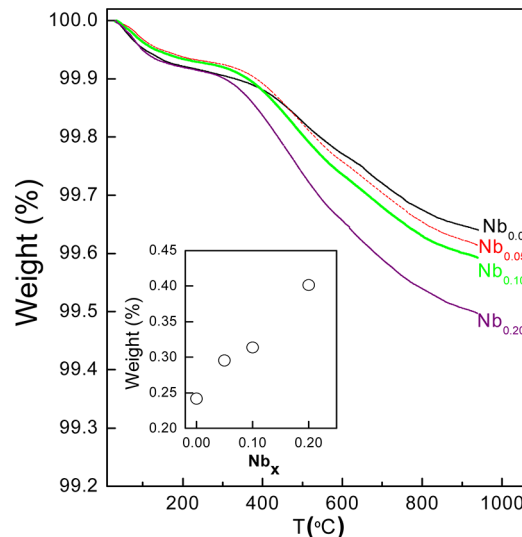


Figure 6. Thermogravimetric curves for $\text{La}_{27}(\text{W}_{1-x}\text{Nb}_x)_5\text{O}_{55.5-5x/2}$ performed under humidified air from 1000°C to room temperature upon cooling. The inset shows the weight uptake from 300 to 800°C as a function of niobium content.

higher than 98%. Weight losses due to possible cation evaporation were not detected during the sintering process. EDS analyses have been performed to confirm the stoichiometry of the sintered specimens. The results presented in Table 2 seem to indicate that no significant deviation from nominal stoichiometry was produced, taking into account that the error in the determination of the concentration of Nb^{5+} is

Table 2. Microanalysis Results, Obtained by EDS, Compared to the Nominal Ratios in Atomic Percentage

	La		W		Nb	
	EDS	nom	EDS	nom	EDS	nom
$\text{Nb}_{0.00}$	83.2(4)	84.4	16.7(4)	15.6	0.0	0.0
$\text{Nb}_{0.025}$	84.6(3)	84.4	15.4(2)	15.2	0.4	0.4
$\text{Nb}_{0.05}$	83.9(8)	84.4	16.0(7)	14.8	0.6(4)	0.8
$\text{Nb}_{0.10}$	82.6(6)	84.4	15.6(3)	14.1	1.6(8)	1.5
$\text{Nb}_{0.15}$	83.6(8)	84.4	14.6(5)	13.3	1.7(6)	2.3
$\text{Nb}_{0.20}$	84.7(6)	84.4	13.5(9)	12.5	1.6(1.0)	3.1
$\text{Nb}_{0.25}$	83.5(9)	84.4	12.7(6)	11.7	4.5(1.3)	3.9

relatively high due to the low atomic concentration of this element (less than 3.9% atomic). The measurements reported in Table 2 correspond to the average of five different microanalyses in the grain interior region of the ceramics. Selected EDS spectra are given in Figure S-2 (Supporting Information) showing the Nb bands which have low intensities but are measurable.

Figure 7a shows the SEM micrograph obtained for a representative sintered pellet with composition $\text{Nb}_{0.10}$. The

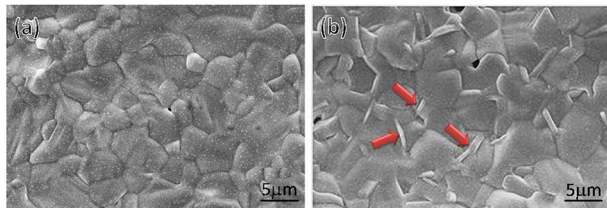


Figure 7. SEM micrograph of the surface of (a) $\text{Nb}_{0.10}$ sintered at 1500 °C for 4 h and (b) $\text{Nb}_{0.30}$ sintered at 1600 °C for 4 h. The arrows in (b) show segregation of La_2O_3 .

pellet exhibits low porosity, and no indications of liquid phase formation or phase segregation at the grain boundaries were observed. The SEM micrographs were analyzed to evaluate the average grain size, which seems to increase slightly with the Nb content between 3.5 μm for Nb_0 to 4.8 μm for $\text{Nb}_{0.2}$. Samples with higher Nb content $x \geq 0.25$ and sintered at 1600 °C show larger grain size, and phase segregations of La_2O_3 were clearly detected at the grain boundary (Figure 7b). The pellet densities were measured before and after the electrochemical measurements obtaining similar results. The $\text{Nb}_{0.25}$ sample containing a low amount of impurity (2.4 wt % of La_2O_3) was stable after the conductivity measurements even under wet atmosphere.

Overall Conductivity. In order to establish the existence of mixed ionic oxide–proton conductivity in the LWNb_x series, an impedance spectroscopy study under a constant flow of dry and wet N_2 , O_2 , and 5% H_2 –Ar gases was carried out. All impedance spectra show three separated contributions at low temperature ascribed to grain interior, grain boundary, and electrode processes, Figure 8. They were fitted by using the following equivalent circuit: $(R_b Q_b)(R_{gb} Q_{gb})Q_e$, where the subscripts b, gb, and e denote grain interior, grain boundary, and electrode processes, respectively; see inset of Figure 8. The resistance of both bulk and grain boundary contributions decreases with increasing the water partial pressure, which confirms the existence of proton conduction in these materials.

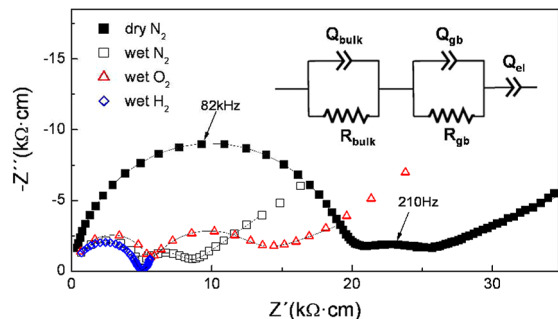


Figure 8. Representative impedance spectra for the $\text{Nb}_{0.2}$ sample under different atmospheres at 250 °C. In the inset is shown the equivalent circuit used to fit the spectra.

A peculiarity related to the grain boundary is that its resistance seems to increase with increasing $p(\text{O}_2)$, and the same behavior was observed in the $\text{La}_{28-y}\text{W}_{4+y}\text{O}_{54+\delta}$ ($\text{La}_{28-y}/\text{W}_{4+y} = 5.5$ –5.7) series. This point needs further investigation to clarify the type of charge carriers dominating at the grain boundary region.

On the other hand, the grain boundary contribution is only visible at relatively low temperatures ($T < 300$ °C) and therefore the bulk conductivity is the main contribution to the overall conductivity at high temperature. This is a major advantage when compared to other proton conducting materials, for instance, Y-doped BaZrO_3 ,^{30–33} which usually exhibits lower overall conductivities due to the large grain boundary resistance.

Figure 9 shows the Arrhenius plots of overall conductivity for the LWNb_x series under different atmospheres. It is clear from that figure that the conductivity in wet atmospheres is always higher than in dry conditions in the whole temperature range studied, indicating that all compounds exhibit proton conductivity. On the other hand, the values of conductivity in wet N_2 are lower than those in wet O_2 due to the larger grain boundary contribution in this last atmosphere as previously commented. In the low temperature range ($T < 500$ °C) the values of activation energy for the overall conductivity increase slightly with Nb content: 62 kJ/mol for $\text{Nb}_{0.0}$, 64 kJ/mol for $\text{Nb}_{0.05}$, and 66 kJ/mol for $\text{Nb}_{0.20}$; these values are close to those previously reported for similar compositions ~60 kJ/mol.³⁴ In the high temperature range the values of overall conductivity increase with increasing the Nb content.

Figure 9c also displays the conductivity of the parent compound “ $\text{La}_6\text{WO}_{12}$ ” with the highest conductivity values reported so far for these lanthanum tungstates.¹⁹ As can be observed, Nb-substitution enhances significantly the ionic conductivity of these materials above 500 °C, while appreciable differences are not observed below this temperature. Taking into consideration that the proton conductivity is predominant at low temperature and similar for the different compositions, the enhancement of conductivity at high temperature could be explained by an increase of the oxide ion conductivity. The slope change in the Arrhenius plots of the conductivity is due to the dehydration of the material, resulting in a conduction mechanism change from predominant protonic at low temperatures to oxide ion at high temperatures. It should be also commented that the incorporation of Nb in the lanthanum tungstate structure seems not to improve the electronic conductivity as confirmed in the next section by studying the overall and electronic conductivity as a function of $p(\text{O}_2)$.

The variation of the overall conductivity in the $\text{La}_{27}(\text{W}_{1-x}\text{Nb}_x)_5\text{O}_{55.5-5x/2}$ series shows a maximum for samples with Nb content between $x = 0.1$ and 0.2, Figure 10. Below 600 °C the proton conductivity is dominant with a significant conductivity change between dry and wet gases. However, above 800 °C the values of conductivity are nearly independent of the atmosphere, suggesting that oxide ion is the main charge carrier. It is clear from this figure that the incorporation of Nb^{5+} in the structure results in a significant enhancement of the ionic conductivity due to an increase of the oxygen vacancy concentration with the highest conductivity values reported for this family of compounds (e.g., 0.01 $\text{S}\cdot\text{cm}^{-1}$ for $\text{Nb}_{0.1}$ and 0.004 $\text{S}\cdot\text{cm}^{-1}$ for Nb_0 at 800 °C).

Conductivity Dependence with $p(\text{O}_2)$. The ionic conductivity for a pure oxide ion conductor is independent of the oxygen partial pressure in a wide range of $p(\text{O}_2)$ values. However, the conductivity increases for a mixed ionic–

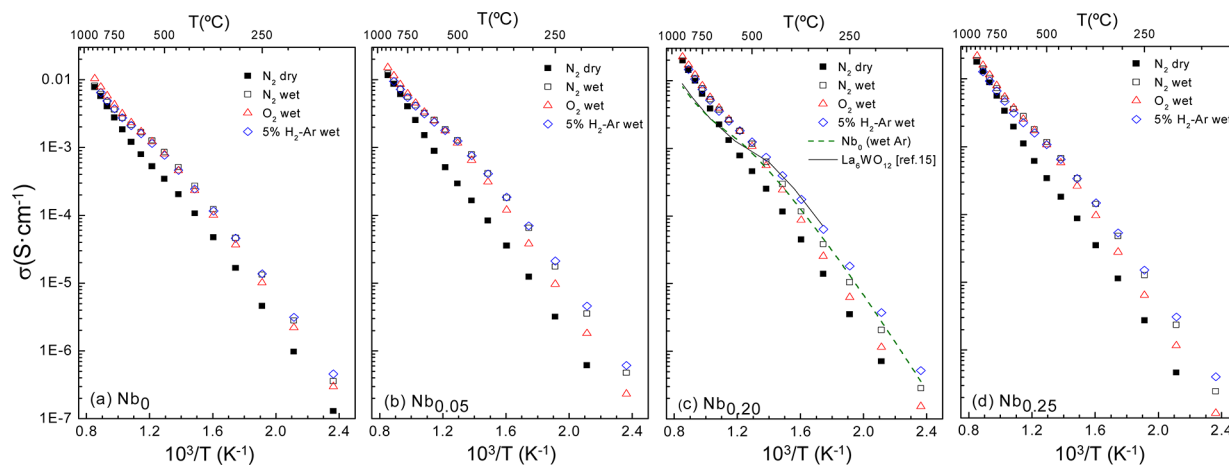


Figure 9. Arrhenius plots of the total conductivity for the $\text{La}_{27}(\text{W}_{1-x}\text{Nb}_x)_5\text{O}_{55.5-5x/2}$ series: (a) $x = 0$, (b) $x = 0.05$, (c) $x = 0.20$, and (d) $x = 0.25$ under various atmospheres. The conductivity of the parent compound “ $\text{La}_6\text{WO}_{12}$ ” from ref 15 is also included for the sake of comparison.

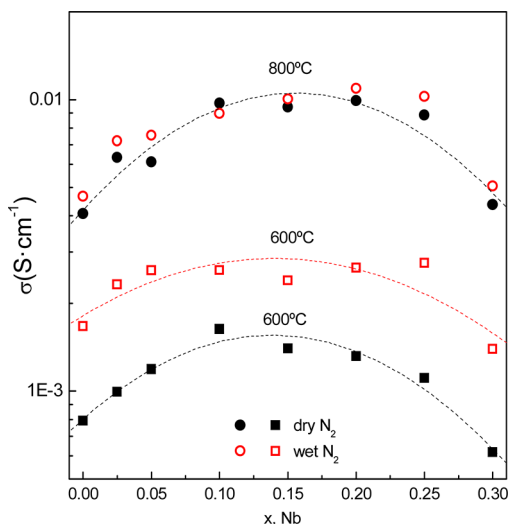


Figure 10. Variation of the overall conductivity for $\text{La}_{27}(\text{W}_{1-x}\text{Nb}_x)_5\text{O}_{55.5-5x/2}$ as a function of the Nb content under dry and wet N₂ at 600 and 800 °C.

electronic conductor as $p(\text{O}_2)$ increases or decreases, depending on the predominant electronic contribution (p- and n-type, respectively). The variation of the overall conductivity for the Nb_{0.10} sample between 800 and 1000 °C as a function of $p(\text{O}_2)$ is shown in Figure 11.

Several conclusions can be drawn from this figure. First, at low temperature and high $p(\text{O}_2)$ range, the conductivity increases slightly with $p(\text{O}_2)$, indicating that the conduction mechanism includes ionic and electron–hole components. Second, the ionic plateau values at intermediate oxygen partial pressure indicate pure ion conduction; third, there is a drop in conductivity at very low reducing conditions.

This last behavior was also observed for nonsubstituted phase Nb₀ and is interpreted based on a decrease in the proton contribution because the oxygen partial pressure is not constant during the experiment.³⁵ It must be highlighted that decreasing the oxygen partial pressure induces a lowering in the water partial pressure. This result also indicates that proton contribution in these materials is significant up to 800 °C, and a similar trend has been already reported for other solid electrolytes, that is, $\text{La}_2\text{Zr}_2\text{O}_7$,³⁶ SrZrO_3 , BaCeO_3 ,^{35,37–39} and Ca_3SiO_5 -based materials.^{40,41} At temperatures higher than 800

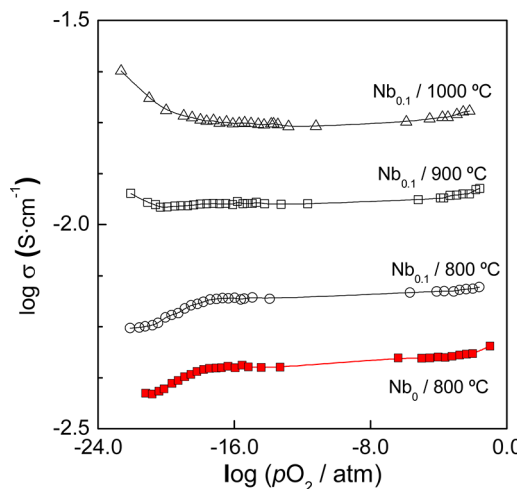


Figure 11. Overall conductivity data at 800, 900, and 1000 °C as a function of oxygen partial pressure for Nb_{0.1} and Nb₀ at 800 °C. The solid line is for visual guidance only.

°C the behavior is consistent with a mixed ionic–electronic conductor with p-type and n-type electronic conductivity at high and low $p(\text{O}_2)$, respectively.

Electronic Conductivity. The electronic conductivity for the sample with composition Nb_{0.20} was estimated by the Hebb–Wagner polarization method. This method assumes that the total electronic conductivity depends on oxygen partial pressure as follows:

$$\sigma_e = \sigma_n^{\text{O}}(P_{\text{O}_2})^{-n} + \sigma_p^{\text{O}}(P_{\text{O}_2})^n \quad (3)$$

where the exponent n is usually equal to 1/4 and σ_n^{O} and σ_p^{O} are the partial n-type and p-type conductivity respectively at the reference oxygen partial pressure. In this case, the electronic current voltage dependence ($I_e - V_s$) obeys the following expression:^{28,29}

$$I_e = \frac{RTS}{FL} \{ \sigma_n^* [\exp(V_s F/RT) - 1] + \sigma_p^* [1 - \exp(-V_s F/RT)] \} \quad (4)$$

where L is the thickness, S the electrode area of the pellet, and F the Faraday constant and σ_n^* and σ_p^* are the n- and p-type electronic conductivities, respectively, at the reference oxygen

partial pressure of the reversible electrode of the polarization cell $p(O_2) = 1$ atm. The electronic current–voltage dependence is shown in Figure 12a. As can be observed, the experimental

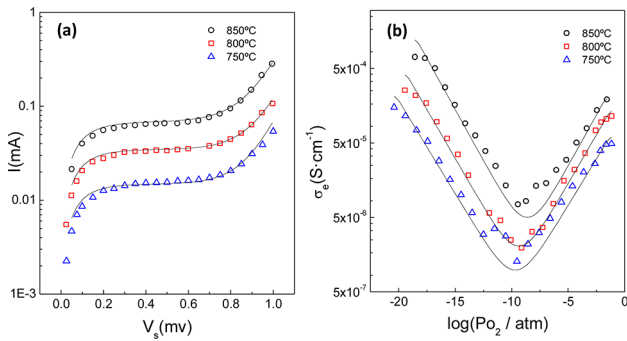


Figure 12. (a) Electronic current–voltage dependence obtained by ion-blocking method and (b) electronic conductivity versus $p(O_2)$ for $Nb_{0.20}$ sample. The solid lines are the fitted results with eq 3.

data fitted reasonably well to eq 3, indicating that the n-type and p-type electronic conductivities have an $\sim 1/4$ power law dependence on the oxygen partial pressure. The variation of the electronic conductivity with the oxygen partial pressure can be obtained from^{28,29}

$$\sigma_e = \left(\frac{L}{S} \right) \frac{dI_e}{dV_S} \quad (5)$$

The electronic conductivity as a function of the oxygen partial pressure is shown in Figure 12b. In agreement with previous reports this material exhibits p- and n-type electronic contributions under oxidizing and reducing atmospheres, respectively.^{16,34} The ionic transport numbers can be estimated by combining the data of electronic conductivity from ion-blocking technique and total conductivity from impedance spectra. The ionic transport numbers for $Nb_{0.10}$ take values of 0.94, 0.98, and 0.99 at 850, 800, and 750 °C, respectively, at $p(O_2) = 10^{-18}$ atm. The activation energies of n- and p-type conductivity, assuming a small polaron hopping mechanism, are approximately ~ 260 and 130 kJ/mol, respectively, which are similar to those estimated previously for n-type conductivity ~ 270 kJ/mol.³⁴ Thus, these materials are mixed ionic–electronic conductors at high temperatures (>800 °C), but below 800 °C the electronic conductivity is negligible and they can be used as PC-SOFC electrolytes as recently confirmed for nonsubstituted lanthanum tungsates.²³

CONCLUSIONS

Single phase oxides belonging to the $La_{27}(W_{1-x}Nb_x)_5O_{55.5-5x/2-\square_{8.5+5x/2}}$ series have been prepared by a freeze-drying precursor method for the Nb compositional range ($0 \leq x \leq 0.2$). The fluorite-related cubic superstructure has been studied by selected area electron diffraction and high-resolution transmission electron microscopy confirming the X-ray powder diffraction results. The thermal analysis study in wet atmosphere showed a higher water uptake for samples with higher oxygen vacancy content. The incorporation of Nb^{5+} increases the oxygen vacancy concentration in the structure and enhances the ionic conductivity: 0.01 S·cm⁻¹ for $Nb_{0.1}$ and 0.004 S·cm⁻¹ for the nonsubstituted Nb_0 phase at 800 °C.

The ionic transport number measurements showed that these materials are mainly ionic conductors below 800 °C.

Above this temperature, these compounds are mixed ionic–electronic conductors displaying both n- and p-type contributions, with transport numbers decreasing from 0.99 to 0.94 as temperature increases from 750 to 850 °C.

ASSOCIATED CONTENT

Supporting Information

Figures S1 and S2 containing variation of crystallographic and experimental densities versus niobium content and EDS spectra. This material is available free of charge via the Internet at <http://pubs.acs.org>.

AUTHOR INFORMATION

Corresponding Author

*E-mail: r_loisilla@uma.es. Telephone: +34-952134234. Fax: +34-952137534.

Notes

The authors declare no competing financial interest.

ACKNOWLEDGMENTS

This work was supported by Junta de Andalucía (Spain) through the P10-FQM-6680 research and Spanish MINECO MAT2010-19837-C06-04.

REFERENCES

- (1) Iwahara, H.; Uchida, H.; Ono, K.; Ogaki, K. *J. J. Electrochem. Soc.* **1988**, *135*, 529–533.
- (2) Iwahara, H.; Esaka. *Solid State Ionics* **1996**, *9*, 86–88.
- (3) Kreuer, K. D. *Annu. Rev. Res.* **2003**, *33*, 333–359.
- (4) Norby, T. *Solid State Ionics* **1999**, *125*, 1–11.
- (5) Bonanos, N.; Knight, K. S.; Ellis, B. *Solid State Ionics* **1995**, *79*, 161–170.
- (6) Iwahara, H.; Yajima, T.; Ushida, H. *Solid State Ionics* **1994**, *70–71*, 267–271.
- (7) Shima, D.; Haile, S. M. *Solid State Ionics* **1997**, *97*, 443–455.
- (8) Chen, F. L.; Toft Sørensen, O.; Meng, G. Y.; Peng, D. K. *J. Eur. Ceram. Soc.* **1998**, *18*, 1389–1395.
- (9) Bonanos, N.; Ellis, B.; Knight, K. S.; Mahmood, M. N. *Solid State Ionics* **1989**, *35*, 179–188.
- (10) Ma, G.; Shimura, T.; Iwahara, H. *Solid State Ionics* **1998**, *120*, 51–60.
- (11) Virkar, A. N.; Maiti, H. S. *J. Power Sources* **1985**, *14*, 295–303.
- (12) Gorbova, E.; Maragou, V.; Medvedev, D.; Demin, A.; Tsikarash, P. *J. Power Sources* **2008**, *181*, 207–213.
- (13) Yoshimura, M.; Baumard, J. F. *Mater. Res. Bull.* **1975**, *10*, 983–988.
- (14) Shimura, T.; Fujimoto, S.; Iwahara, H. *Solid State Ionics* **2001**, *143*, 117–123.
- (15) Haugsrud, R. *Solid State Ionics* **2007**, *178*, 555–560.
- (16) Haugsrud, R.; Kjølseth, K. *J. Phys. Chem. Solids* **2008**, *69*, 1758–1765.
- (17) Escolástico, S.; Vert, V. B.; Serra, J. M. *Chem. Mater.* **2009**, *21* (14), 3079–3089.
- (18) Haugsrud, R.; Fjeld, H.; Haug, K. R.; Norby, T. *J. Electrochem. Soc.* **2007**, *154* (1), B77–B81.
- (19) Magrasó, A.; Frontera, C.; Marrero-López, D.; Núñez, P. *Dalton Trans.* **2009**, 10273–10283.
- (20) Lashtabeg, A.; Bradley, J.; Dicks, A.; Auchterlonie, G.; Drennan, J. *J. Solid. State. Chem.* **2010**, *183* (5), 1095–1101.
- (21) Escolástico, S.; Solis, C.; Serra, J. M. *Solid State Ionics* **2012**, *216*, 31–35.
- (22) Escolástico, S.; Solis, C.; Serra, J. M. *Int. J. Hydrogen Energy* **2011**, *36*, 11946–11954.
- (23) Solis, C.; Navarrete, L.; Roitsch, S.; Serra, J. M. *J. Mater. Chem.* **2012**, *22*, 16051–16059.

- (24) Magrasó, A.; Polfus, J. M.; Frontera, C.; Canales-Vázquez, J.; Kalland, L.-E.; Hervoches, C. H.; Erdal, S.; Hancke, R.; Islam, M. S.; Norby, T.; Haugsrud, R. *J. Mater. Chem.* **2012**, *22* (5), 1762–1764.
- (25) Amsif, M.; Magrasó, A.; Marrero-López, D.; Ruiz-Morales, J. C.; Canales-Vázquez, J.; Nuñez, P. *Chem. Mater.* **2012**, *24*, 3868–3877.
- (26) Larson, A. C.; Dreele, R. B. V. *General Structure Analysis System (GSAS) program*; Rep. No. LA-UR-86748; Los Alamos National Laboratory: Los Alamos, CA, 1994.
- (27) Johnson, D. *ZView: a Software Program for IES Analysis*, Version 2.8; Scribner Associates, Inc.: Southern Pines, NC.
- (28) Hebb, M. H. *J. Chem. Phys.* **1952**, *20*, 185–190.
- (29) Marrero-López, D.; Canales-Vázquez, J.; Ruiz-Morales, J. C.; Irvine, J. T. S.; Nuñez, P. *Electrochim. Acta* **2005**, *50*, 4385–4395.
- (30) Kjolseth, C.; Fjeld, H.; Prytz, Ø.; Dahl, P. I.; Estournès, C.; Haugsrud, R.; Norby, T. *Solid State Ionics* **2010**, *181* (5–7), 268–275.
- (31) Babilo, P.; Uda, T.; Haile, S. M. *J. Mater. Res.* **2007**, *22* (5), 1322–1330.
- (32) Duval, S. B. C.; Holtappels, P.; Vogt, U. F.; Pomjakushina, E.; Conder, K.; Stimming, U.; Graule, T. *Solid State Ionics* **2007**, *178* (25–26), 1437–1441.
- (33) Kreuer, K. D. *Annu. Rev. Res.* **2003**, *33*, 333–359.
- (34) Erdal, S.; Kalland, L.-E.; Hancke, R.; Polfus, J.; Haugsrud, R.; Norby, T.; Magrasó, A. *Int. J. Hydrogen Energy* **2012**, *37* (9), 8051–8055.
- (35) Labrincha, J. A.; Marques, F. M. B.; Frade, J. R. *J. Mater. Sci.* **1995**, *30*, 2785–2792.
- (36) Labrincha, J. A.; Frade, J. R.; Marques, F. M. B. *Solid State Ionics* **1997**, *99*, 33–40.
- (37) Labrincha, J. A.; Frade, J. R.; Marques, F. M. B. *Solid State Ionics* **1993**, *61*, 71–75.
- (38) Yamija, T.; Susuki, H.; Yogo, T.; Iwahara, H. *Solid State Ionics* **1992**, *51*, 101–107.
- (39) Iwahara, H.; Uchida, H.; Ono, K.; Ogaki, K. *J. Electrochem. Soc.* **1988**, *135*, 529–533.
- (40) Porras-Vázquez, J. M.; de la Torre, A. G.; Marrero-López, D.; Losilla, E. R.; Aranda, M. A. G. *Dalton Trans.* **2006**, 2691–2697.
- (41) Porras-Vázquez, J. M.; de la Torre, A. G.; Losilla, E. R.; Aranda, M. A. G. *Solid State Ionics* **2007**, *178*, 1073.